Chasing Schottky–Mott: Metal-first non-alloyed contacts to β-Ga$_2$O$_3$ for interface quality and minimal surface modification ⒺⓅ

Kathleen T. Smith,[1,a] ⓘD Cameron A. Gorsak,[2] ⓘD Joshua T. Buontempo,[2] ⓘD Bennett J. Cromer,[2] ⓘD
Takumi Ikenoue,[3] ⓘD Hemant Gulupalli,[2] ⓘD Michael O. Thompson,[2] ⓘD Debdeep Jena,[2,4,5] ⓘD Hari P. Nair,[2] ⓘD
and Huili Grace Xing[2,4,5,a] ⓘD

AFFILIATIONS

[1]School of Applied and Engineering Physics, Cornell University, Ithaca, New York 14853, USA
[2]Department of Materials Science and Engineering, Cornell University, Ithaca, New York 14853, USA
[3]Graduate School of Energy Science, Kyoto University, Kyoto 606-8501, Japan
[4]School of Electrical and Computer Engineering, Cornell University, Ithaca, New York 14853, USA
[5]Kavli Institute at Cornell for Nanoscale Science, Cornell University, Ithaca, New York 14853, USA

[a]Authors to whom correspondence should be addressed: kts57@cornell.edu and grace.xing@cornell.edu

ABSTRACT

Metal-first non-alloyed ohmic and Schottky contacts are fabricated on β-Ga$_2$O$_3$ with a range of metal work functions (ϕ_M). The resulting ohmic contacts are of high quality with a contact resistance (R_c) as low as $0.069 \pm 0.003 \, \Omega$ mm. Measurements of the barrier heights (ϕ_B) indicate that metal-first processing, which preserves the as-grown/bare-substrate surface, also partially un-pins the Fermi-level in (010) and ($\bar{2}$01) oriented Ga$_2$O$_3$. Depth-resolved XPS (x-ray photoelectron spectroscopy) measurements of the oxidation state throughout the contact metal at the contact–Ga$_2$O$_3$ interface indicate that most non-alloyed contact metals are at least partially oxidized by room temperature redox reactions with the underlying Ga$_2$O$_3$, with metals with a lower ϕ_M also demonstrating the greatest level of oxidation. As oxidation has been previously observed to enhance a metal's work function, this may imply that to-date observations of indices of surface behavior $<< 1$ on β-Ga$_2$O$_3$, which have been attributed to severe Fermi-level pinning, may need to be corrected to account for this partial oxidation in addition to other surface modifications during device processing demonstrated in this work.

I. INTRODUCTION

Beta-phase gallium-oxide (β-Ga$_2$O$_3$) has been investigated in recent years as a promising material in power electronics thanks to its large estimated critical breakdown field (8 MV/cm), adequate electron mobility (200 cm^2/V s), and availability of large area substrates from melt.[1–3] Impressive devices demonstrations have been recorded with a record average breakdown electric field observed in both Schottky barrier diodes (SBDs) and field-effect transistors (FETs) at 5.7 MV/cm, with surface fields as high as 6 MV/cm enabled by oxidized metal Schottky contacts with barrier heights (ϕ_B) > 2 eV.[4–7]

Despite these advances, reported Schottky-barrier heights to Ga$_2$O$_3$ through the years have demonstrated a stark lack of consistency.[8] The Schottky-barrier height at a metal–semiconductor interface is nominally defined by the Schottky–Mott rule, where the barrier height is determined only by the electron affinity of the semiconductor (χ_S) and the work function of the metal (ϕ_M) according to Eq. (1),

$$\phi_B = \phi_M - \chi_S. \tag{1}$$

However, experimental results have deviated from this expectation. For example, a Pt ($\phi_M \sim 5.65$ eV) to Ga$_2$O$_3$ ($\chi_S \sim 3.9$ eV) contact is predicted to have a ϕ_B of 1.6–1.75 eV. Nevertheless, reported values range between 0.6 and 2.2 eV.[9,10] The deviation of

ϕ_B from the Schottky–Mott rule has been attributed to Fermi-level pinning. Furthermore, while some studies suggest that the Fermi level is fully pinned in Ga_2O_3, others have demonstrated that ϕ_B is only weakly pinned as predicted by Kurtin *et al.* given the ionicity of Ga_2O_3, which is not high enough to yield the complete pinning observed in GaAs.[11] This partial surface pinning has been observed in other semiconducting materials, and thus, an index of surface behavior (S) was introduced to describe Fermi-level pinning, which modifies the Schottky–Mott rule to[12]

$$\phi_B = S\phi_M - \chi_S, \qquad (2)$$

where $S = 1$ corresponds to ideal Schottky–Mott behavior and $S = 0$ corresponds to a fully pinned surface. Fermi-level pinning in $\beta\text{-}Ga_2O_3$ has been attributed to a number of origins, including the surface orientation, native oxygen and gallium vacancies or interstitials induced during growth, and surface defects generated during device fabrication processes, such as high temperature annealing and energetic plasma exposure.[8]

Our previous work has demonstrated that conventional lift-off processing of metal contacts significantly modifies the surface of $\beta\text{-}Ga_2O_3$ and impedes consistent and reliable ohmic contact formation, while a metal-first contact process improves both contact quality and consistency.[13] Contact-first processes have also been demonstrated in prior studies, albeit not explicitly for the purpose of minimal surface modification, in ITO/AZO ohmic contacts that outperformed conventional lifted-off Ti/Au contacts reported by Carey *et al.*, and in the ozone-MBE deposited oxidized Schottky contacts that attained 6 MV/cm reported by Cromer *et al.*[7,14,15] Given nearly all metal contacts to Ga_2O_3 in the literature to date were formed by lift-off, it is reasonable to assume the same or similar processing inconsistencies observed in Ti/Au ohmic contacts (Ref. 13) may have led to the wildly varied values of ϕ_B and S in the literature.

In this work, we demonstrate non-alloyed, metal-first ohmic and Schottky contacts fabricated with contact metals having a range of work functions to further explore the limitations of Fermi-level pinning in $\beta\text{-}Ga_2O_3$. We fabricated transfer length method (TLM) patterns for all six contact metals (Al, Ti, Cr, Ni,

Pd, and Pt) and vertical SBDs for the high work-function metals (Ni, Pd, and Pt) and, by fitting the ohmic and Schottky IV behavior of these contacts to established emission mechanisms, are able to extract apparent specific contact resistances for metal contacts that exhibit ohmic IV characteristics and Schottky-barrier heights for both ohmic and Schottky characteristics.

II. METHODS

The TLM patterns for all six contact metals were fabricated on two heavily n+ doped samples grown by metal–organic chemical vapor deposition (MOCVD), each diced into three pieces after growth to reduce inter-sample growth non-uniformity (samples A–F). The *in situ* doped samples were grown in an Agnitron Agilis 100 MOCVD system on Fe-doped (010) $\beta\text{-}Ga_2O_3$ substrates. Prior to growth, samples were *ex situ* etched with 48% HF for 30 min and immediately loaded.[16] A 50 nm unintentionally doped buffer layer was grown first before growing the 220–250 nm highly doped layer. The samples were then diced and solvent cleaned. Further details of the MOCVD growth can be found in the supplementary material. Hall measurements on previously grown calibration samples gave a channel charge and mobility of 9×10^{19} cm^{-3} and 84 cm^2/V s for samples A, D, and F and 7×10^{19} cm^{-3} and 89 cm^2/V s for samples B–C and E. The metal stacks were then deposited by electron-beam evaporation. Circular TLM (CTLM) patterns were defined using contact lithography, and the metal stacks were then wet etched (see Table I for metal layer thicknesses and wet etch conditions). The detailed fabrication of metal-first ohmic contacts can be found in our prior report.[13]

The SBDs for the high work-function metals were fabricated on diced 1×1 cm^2 pieces (samples G–I) from a 2 in. ($\bar{2}01$) Sn-doped $\beta\text{-}Ga_2O_3$ substrate from Novel Crystal Technology, Inc. The fabrication process is diagrammed in Fig. S1 of the supplementary material, including a blanket backside ohmic contact, frontside blanket deposition of the Ni, Pd, or Pt followed by photolithographic and wet etch anode patterning, and a BCl_3/Cl_2-based self-aligned mesa etch for isolation. During backside cathode deposition, the front side of the sample was protected

TABLE I. Summary of metal/Ga_2O_3 samples in this study: metal stacks, nominal work function of the contact metal, and metal etch conditions.

Sample	orientation	N_d (cm^{-3})	Metal Stack (nm)	ϕ_M (eV)	Etchant 1	Etch 1 Time (s)	Etchant 2	Etch 2 Time (s)
Ohmic series								
A	(010)	9×10^{19}	Al (110)	4.2	Al etchant, type A	210	…	…
B	(010)	7×10^{19}	Ti/Au (10/110)	4.33	Gold etchant TFA	40	30:1 BOE	90
B′	(010)	9×10^{19}	Ti/Au (10/110)	4.33	Gold etchant TFA	40	30:1 BOE	90
C	(010)	7×10^{19}	Cr/Au (10/110)	4.5	Gold etchant TFA	40	Cr Etch 1020	20
D	(010)	9×10^{19}	Ni/Au (10/110)	5.2	Gold etchant TFA	40	1:1 DI:HCl, 35 °C	60
E	(010)	7×10^{19}	Pd/Au (10/110)	5.4	Gold etchant TFA	40	…	…
F	(010)	9×10^{19}	Pt/Au (10/110)	5.65	Gold etchant TFA	40	200 V ion mill	120
SBD series								
G	($\bar{2}01$)	$\sim 6 \times 10^{18}$	Ni/Au (10/110)	5.2	Gold etchant TFA	40	1:1 DI:HCl, 35 °C	60
H	($\bar{2}01$)	$\sim 6 \times 10^{18}$	Pd/Au (10/110)	5.4	Gold etchant TFA	40	…	…
I	($\bar{2}01$)	$\sim 6 \times 10^{18}$	Pt/Au (10/110)	5.65	Gold etchant TFA	40	200 V ion mill	120

by a blanket layer of photoresist. The protective layer was removed before cathode annealing by a long soak (>30 min) in heated (~65 °C) 1165 Microposit Remover™. Coating and removal of a blanket photoresist layer by solvent strip has been demonstrated to still form uniform, low resistance metal-first Ti/Au ohmic contacts on n+ β-Ga$_2$O$_3$, sample B′. The process information for sample B′ is included in Table I, with full process information detailed in the supplementary material. An additional solvent clean in acetone and isopropanol was performed prior to frontside anode deposition. Full process details are included in the supplementary material.

The CTLM patterns were measured using a Keithley 4200 Semiconductor Characterization System in a four-point probe configuration, with an inner radius of 50 μm and TLM pad spacings from 3 to 12 μm confirmed by scanning electron microscopy. Forward I–V, reverse I–V, and C–V were measured on the SBDs using the same system in a vertical two-point configuration on devices with an anode radius of 100 μm. A Thermo-Nexsa G2 x-ray photoelectron spectrometer (XPS) with Al-Kα x-ray source with *in situ* ion mill and electron flood gun for charge compensation was used to measure the oxidation state of the metal contact at the metal–semiconductor interface.

III. EXPERIMENTAL RESULTS: OHMIC CONTACTS

Figure 1(a) shows the I–V curves from an example CTLM pattern with 5 μm spacing for samples A–F. The low work-function contacts (samples A–C) are linear or nearly linear ohmic with the resistance apparently increasing with increasing ϕ_M of the contact metal from Al (ϕ_M = 4.2 eV) to Cr (ϕ_M = 4.5 eV). The high work-function metals (samples D–F) show varying degrees of Schottky behavior. From sampling at least four sets of TLM patterns per

sample, we find that the Al contacts have an average non-alloyed R_c of 0.069 ± 0.003 Ω mm, which leads to a specific contact resistance (ρ_c) of 1.1 ± 0.1 × 10^{-6} Ω-cm^2 [Figs. 1(b)–1(c)]. Notably, R_c is constant over the entire 100 mA measurement range [Fig. 1(b)]. This is among the lowest reported contact resistances on (010) β-Ga$_2$O$_3$. These Al-based contacts, as well as the Ti and Cr contacts, are benchmarked in Fig. 2. Further improvements in contact resistance can be anticipated by increasing to doping densities beyond 1 × 10^{20} cm^{-3} and by refining surface cleanliness. Thermal stability of these metal-first interfaces also remains an open question beyond the scope of this work.

The Ti and Cr contacts on samples B and C have a higher average non-alloyed R_c of 0.48 ± 0.01 Ω-mm and 0.80 ± 0.01 Ω-mm, respectively, with a corresponding ρ_c of 2.9 ± 0.1 × 10^{-5} Ω cm^2 and 1.1 ± 0.1 × 10^{-4} Ω cm^2. These results are summarized in Table II. The Ti/Au contacts on sample B′ are also linear and ohmic, with a non-alloyed R_c and corresponding ρ_c of 0.18 ± 0.01 Ω-mm and 6.5 ± 0.6 × 10^{-6} Ω-cm^2, respectively. These contacts are also included in Table II and Fig. 2, with a full discussion of the contact behavior included in the supplementary material. The Ni, Pd, and Pt contacts do not show linear I–V behavior, and thus, a contact resistance is not extracted.

A. Relating barrier height and contact resistance

At zero bias, the specific contact resistance is determined from the J–V behavior of the contact according to[18]

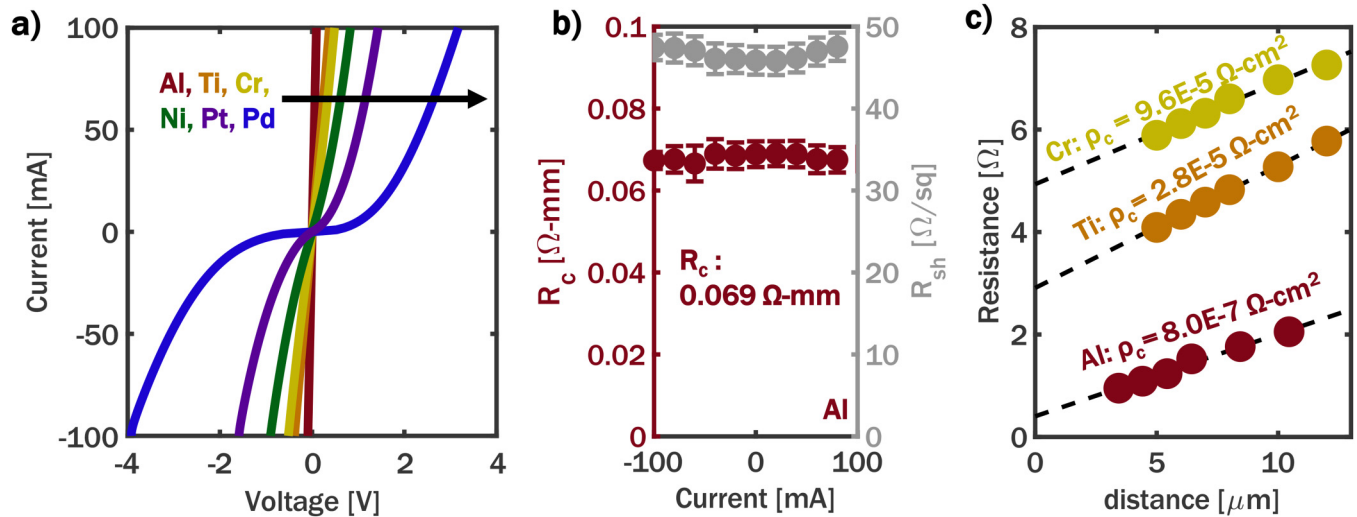$$\rho_c \equiv \left(\frac{dJ}{dV} \right)^{-1}_{V=0}. \tag{3}$$

FIG. 1. (a) I–V curves for an example CTLM pattern with a 5 μm spacing for Al (red), Ti (orange), Cr (yellow), Ni (green), Pd (blue), and Pt (purple) contacts. Al and Ti have linear ohmic behavior, while Cr has nearly-linear ohmic behavior. Ni, Pd, and Pt all have Schottky I–V behavior. (b) Extraction of R_c and R_{sh} for Al contacts from 0 to 100 mA applied current bias. R_c is effectively constant at 0.069 ± 0.003 Ω mm (1.1 ± 0.1 × 10^{-6} Ω cm^2) after averaging over four sets of CTLM patterns. (c) Extraction of ρ_c at 0 mA applied bias for Al, Ti, and Cr contacts on an example CTLM set gives 0.063 Ω mm (8.0 × 10^{-7} Ω cm^2), 0.46 Ω mm 2.8 × 10^{-5} (Ω cm^2), and 0.77 Ω mm (9.6 × 10^{-5} Ω cm^2), respectively.
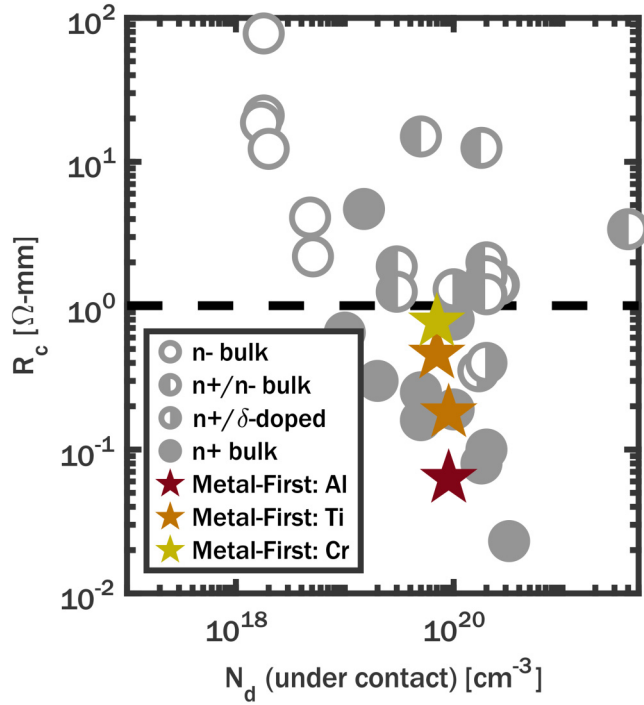
FIG. 2. Benchmarking of Al, Ti, and Cr ohmic contacts to (010) β-Ga$_2$O$_3$. The historical data used in this plot are tabulated in the supplementary material.

In order to apply this relation to our ohmic contacts, we must first determine which mechanism dominates forward conduction at low applied bias. As all the metal contacts fabricated here, regardless of I–V behavior, ought to exhibit a Schottky barrier, we have three mechanisms to consider: thermionic emission (TE) over the barrier, field emission (FE) tunneling through the barrier, or thermionic-field emission (TFE), which combines the two. We can then identify the appropriate expression for J. The criteria used to distinguish between conduction regimes is typically related to the surface electric field (F_{surf}). As ρ_c is reported here at 0 bias, we will reference our criteria to the surface electric field at 0 bias, F_0, which is given by[19]

$$F_0 = \sqrt{\frac{2(N_d - N_a)(qV_{bi} - k_BT)}{\epsilon_s}}, \qquad (4)$$

with ϵ_s, k_B, T, and N_d assuming their typical meanings and V_{bi} being the built-in voltage. Often, a simplified version of V_{bi}, $V_{bi,0} = \phi_B$ is used. However, for degenerately doped semiconductors, additional considerations must be made.

B. Calculating built-in potential

In degenerate semiconductors, E_f lies above E_c. The normally unoccupied states above the conduction band minimum but below E_f are occupied by electrons, i.e., the Burstein–Moss (BM) band filling effect (ΔE_{BM}), leading to an expansion in the optical absorption bandgap ($E_{g,opt}$). In addition, bandgap renormalization ($\Delta E_{BGR} = \Delta E_{BGR,C} + \Delta E_{BGR,V}$) occurs due to electron–electron (ΔE_{ee}) and electron–dopant (ΔE_{ei}) Coulomb interactions, which narrow the bandgap.[17,20] Both BM band filling and bandgap renormalization (BGR) depend on doping concentration. Figure 3(a) sketches the impacts of both of these effects on the semiconductor band structure. The expressions for ΔE_{BM} and ΔE_{BGR} are described in the supplementary material and plotted in Fig. S2 of the supplementary material. However, the net optical absorption bandgap plotted in Fig. S2 of the supplementary material is not the critical parameter in this study, but instead (1) V_{bi}, which is determined by the relative difference between ϕ_M and E_f in the *bulk* Ga$_2$O$_3$, and (2) ϕ_B, which is controlled by the location of the conduction band edge E_c relative to ϕ_M at the *contact interface*. To address the first question, from the band diagram of

TABLE II. Summary of extracted barrier heights for metal/Ga$_2$O$_3$ interfaces in this work.

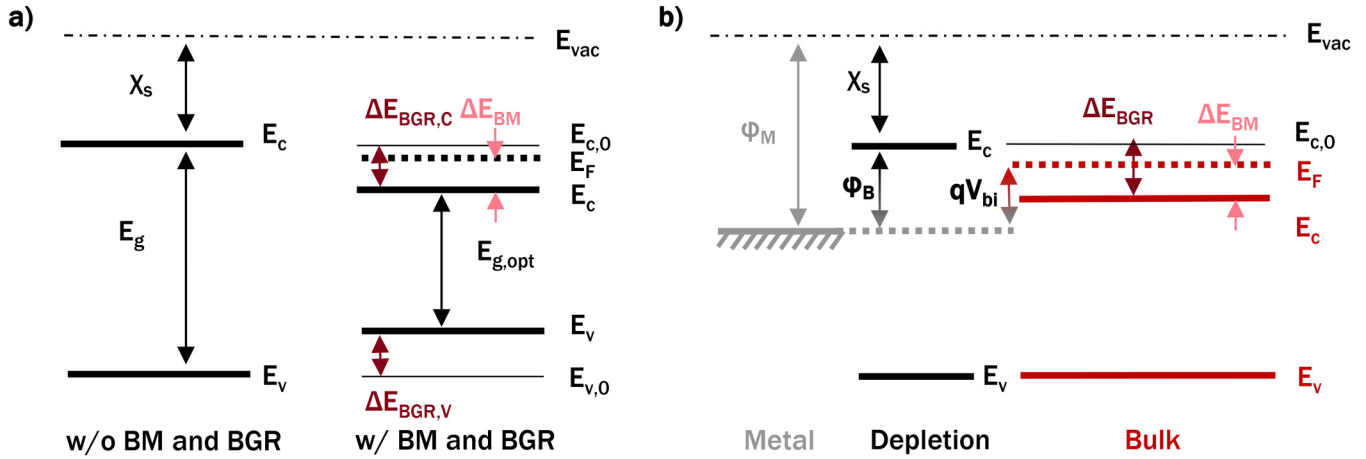| Ohmic series					
Sample	Contact metal	ϕ_M (eV)	$\phi_{B,FIV}$ (eV)	R_c (Ω mm)	ρ_c (Ω cm^2)
A	Al	4.2	0.27 ± 0.03	0.069 ± 0.003	1.1 ± 0.1×10^{-6}
B	Ti	4.33	0.57 ± 0.01	0.48 ± 0.01	2.9 ± 0.1×10^{-5}
B′	Ti	4.33	0.59 ± 0.01	0.18 ± 0.01	6.5 ± 0.6×10^{-6}
C	Cr	4.5	0.69 ± 0.01	0.80 ± 0.01	1.1 ± 0.1×10^{-4}
SBD series					
				$\phi_{B,RIV}$ (eV)	$\phi_{B,CV}$ (eV)
G	Ni	5.2	1.08 ± 0.12	1.10 ± 0.11	1.31 ± 0.01
H	Pd	5.4	1.46 ± 0.02	1.44 ± 0.01	1.71 ± 0.25
I	Pt	5.65	1.32 ± 0.02	1.33 ± 0.02	1.43 ± 0.11

FIG. 3. Illustrative diagrams (not to scale) (a) with and without the Burstein–Moss effect and bandgap renormalization applied. The BM shift occurs entirely in the conduction band, while band renormalization ($\Delta E_{BGR} = \Delta E_{BGR,C} + \Delta E_{BGR,V}$) is divided between the conduction and valence bands (not necessarily evenly). The new optical absorption bandgap is measured from the valence band maximum to the Fermi level due to Burstein–Moss. (b) Band diagram showing the band structure in the metal contact, the depletion region, and semiconductor bulk taking into account BM and BGR in degenerate semiconductors. BGR is only applied in the bulk due to a lack of electron–electron interactions in the depletion region and is sketched only in the conduction band due to the observations made by Zhang *et al.* from DFT.[17] The new V_{bi} is also highlighted.

the bulk in Fig. 3(b), we can quickly observe that

$$qV_{bi} = \phi_B - \Delta E_{BGR,C} + \Delta E_{BM} = qV_{bi,0} - \Delta E_{BGR} + \Delta E_{BM}, \quad (5)$$

with $V_{bi,0}$ being the built-in potential of the metal–semiconductor junction if E_f of the semiconductor bulk is at $E_{c,0}$—a common assumption made for a degenerate semiconductor. The quantities ΔE_{BM} and ΔE_{BGR} are described in the supplementary material.

As for the second point, Zhang *et al.* further carried out hybrid DFT calculations and determined that the conduction band edge is minimally impacted by bandgap renormalization resulting from electron-impurity interactions (ΔE_{ei}) due to minimal hybridization between the Si 3s and Ga 4s state that forms the basis of the conduction band minimum.[17] Therefore, all bandgap renormalization (ΔE_{BGR}) may be attributed to electron–electron interactions (ΔE_{ee}). As electron–electron interactions are largely absent in the depletion region near the metal–semiconductor contact interface, we anticipate no bandgap renormalization at the interface, and therefore, the location of E_c relative to ϕ_M (and, therefore, ϕ_B) is unaffected. In the bulk, bandgap renormalization is predominantly seen through lowering of the conduction band minimum due to the dispersive Ga 4s state from which the conduction band is derived compared to the flat valence band edge. Thus, $\Delta E_{BGR} = \Delta E_{BGR,C}$ for n+ Ga$_2$O$_3$ doped with Si and is sketched entirely in the conduction band in Fig. 3(b).[17]

C. Meeting criteria for thermionic-field emission

With V_{bi} and F_0 established, we can now apply the electric field criteria to determine which conduction regime applies to our contacts: TE, TFE, or FE. In the FE dominated current region,

Padovani and Stratton's criteria requires that[21]

$$\frac{F}{F_0} > \sqrt{\frac{q\phi_B}{k_B T}}. \quad (6)$$

As we determine contact resistance near zero bias, $F \sim F_0$ and TFE will dominate over FE as long as $q\phi_B >$ several $k_B T$. With such low barrier heights predicted by Schottky–Mott, it is then important to distinguish whether TFE or TE current dominates. To determine the appropriate conduction regime, we use the transition electric field F_T described by Li *et al.* for Ga$_2$O$_3$ below which TE dominates,[19]

$$F_T = 0.70 \cdot T^2 + 780 \cdot T - 3.0 \times 10^4 \, \text{V/cm}. \quad (7)$$

At the doping concentrations used for this study ($> 5 \times 10^{19} \, \text{cm}^{-3}$), $F_0 > F_T$ holds even for barriers as small as $1.15 \times k_B T$ or 30 meV at room temperature. Even at 600 K, the cutoff for ϕ_B to transition from the TE to TFE regime is $1.4 \times k_B T$ or 36 meV at room temperature. These criteria are shown in Fig. S2 of the supplementary material. Based on these criteria, the dominant mode of conduction in the ohmic contacts in this study is TFE. The TFE model for the current density under forward bias V_F is laid out in Eqs. (8)–(10), with A^* being Richardson's constant for Ga$_2$O$_3$,[21,22]

$$J_{TFE} = \frac{A^* T \sqrt{\pi E_{00}(\phi_B - qV_F + \xi_2)}}{k_B \cosh(E_{00}/k_B T)}$$
$$\times \exp\left(\frac{\xi_2}{k_B T} - \frac{\phi_B + \xi_2}{E_0}\right) \exp\left(\frac{qV_F}{E_0}\right), \quad (8)$$

$$E_{00} = \frac{q\hbar}{2}\sqrt{\frac{N_d}{m^*\epsilon_s}}, \tag{9}$$

$$E_0 = E_{00}\coth\left(\frac{E_{00}}{k_BT}\right). \tag{10}$$

In Eq. (9), we use the modified expression for m^* described in the supplementary material due to mild nonparabolicity in the conduction band. In the original TFE formulation by Padovani and Stratton, the BM band filling energy ξ_2 is considered, while the effect of BGR is neglected; thus, $V_{bi} = V_{bi,0} + \xi_2$. However, in this study, it is necessary to consider the BGR effect as it is sizable in comparison with the barrier height (<1 eV) we expect from the ohmic contact characteristics. We correct the expression for V_{bi} according to Eq. (5) to account for this effect, from which we see that

$$\xi_2 = \Delta E_{BM} - \Delta E_{BGR,C} = \Delta E_{BM} - \Delta E_{BGR}. \tag{11}$$

D. Extracting barrier height from contact resistance

By applying Eq. (3), J_{TFE} can be used to attain an expression for $\rho_{c,TFE}$, substituting for ξ_2 according to Eq. (11),[18]

$$\rho_{c,TFE} = \frac{k_B\sqrt{E_{00}}\cosh(E_{00}/k_BT)\coth(E_{00}/k_BT)}{A^*Tq\sqrt{\pi(q\phi_B + \Delta E_{BM} - \Delta E_{BGR})}}$$
$$\times \exp\left(\frac{q\phi_B + \Delta E_{BM} - \Delta E_{BGR}}{E_{00}\coth(E_{00}/k_BT)} - \frac{\Delta E_{BM} - \Delta E_{BGR}}{k_BT}\right). \tag{12}$$

Using the extracted specific contact resistance from TLM, ϕ_B can be solved for numerically. We attain barrier heights for Al, Ti, and Cr of 0.29 ± 0.03, 0.57 ± 0.01, and 0.69 ± 0.01 eV, respectively. These, and all extracted barrier heights, are listed in Table II. The values of ϕ_B monotonically increase with increasing ϕ_M. Similar analysis applied to Ti contacts on 3×10^{19}, 7×10^{19}, and 8×10^{19} cm^{-3} Si-doped β-Ga$_2$O$_3$ reported in our previous work yields similar barrier heights of 0.60, 0.54, and 0.56 eV, respectively, to the extracted ϕ_B for Ti of 0.57 eV reported here.[13]

Neglecting both BM and BGR (i.e., setting E_f at E_c in the bulk ignoring renormalization effects, as is commonly assumed for degenerate semiconductors), the extracted ϕ_B is ~40 meV higher than the values extracted here as, at doping densities $\sim 5-10 \times 10^{19}$ cm^{-3}, the competing effects of BM and BGR on V_{bi} are approximately equal in magnitude and, therefore, nearly cancel out. Including BM but neglecting BGR, which is most commonly seen in the literature when applying the equation by Padovani and Stratton, leads to significantly larger barrier heights by ~0.5–0.6 eV due to the artificial increase in V_{bi}.

IV. EXPERIMENTAL RESULTS: SCHOTTKY CONTACTS

For the rectifying Ni, Pt, and Pd contacts, we fabricated SBDs to extract barrier height and used three different methods to extract the barrier height: C–V, forward J–V fitted with the TFE model, and reverse J–V fitted with a numerical tunneling model developed by Li et al.[19,23] The room temperature C–V measurements are fit

according to Eq. (13) with $\epsilon_s = 10\epsilon_0$ for β-Ga$_2$O$_3$ and N_d and $\phi_{B,CV}$ as fitting parameters,

$$\frac{1}{C^2} = \frac{-2}{qN_d\epsilon_sA^2}V + \frac{2}{qN_d\epsilon_sA^2}\phi_{B,CV}. \tag{13}$$

The extracted N_d and $\phi_{B,CV}$ were 5.58×10^{18} cm^{-3} and 1.31 ± 0.01 eV for Ni, 6.93×10^{18} cm^{-3} and 1.71 ± 0.25 eV for Pd, and 6.52×10^{18} cm^{-3} and 1.43 ± 0.11 eV for Pt.

The forward J–V characteristics of the diodes in the exponential region are fit with the TFE model according to Eqs. (8)–(10), with N_d set to the value extracted by C–V, V_F as the independent variable, and $\phi_{B,FIV}$ as the only fitting parameter. The agreement of forward J–V characteristics and the TFE model is shown in Fig. 4(b). The extracted values of $\phi_{B,FIV}$ for Ni, Pd, and Pt are 1.08 ± 0.12, 1.46 ± 0.02, and 1.32 ± 0.02 eV, respectively. Unlike for the heavily degenerately doped ohmic contacts, neglecting BM and/or BGR results in a minimal shift (~20 meV) in the extracted ϕ_B as the doping density in these samples is similar to the conduction band density of states in β-Ga$_2$O$_3$, meaning that the samples are barely degenerately doped and $E_f = E_c$ is a reasonable approximation.

The reverse J–V characteristics of the SBDs are fit using the numerical reverse leakage model developed by Li et al. (described in the supplementary material), which incorporates doping effects and image force lowering (IFL) into the models developed by Murphy and Good and expanded by Padovani and Stratton.[19,21,24] For fitting to the measured reverse J–V characteristics, V_R is related to F_{surf} according to $F_{surf} = \sqrt{2qN_d(\phi_{B,RIV} - V_R)/\epsilon_s}$, with N_d again set to the value extracted from C–V. This leaves V_R as the independent variable and $\phi_{B,RIV}$ as the only fitting parameter. The

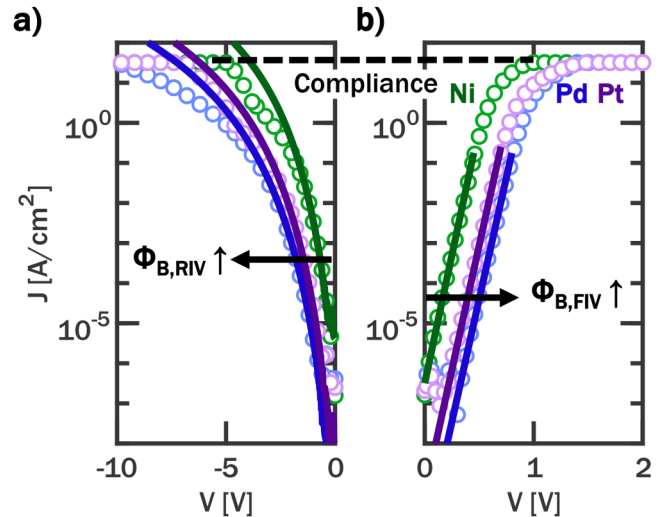<div style="writing-mode: vertical-rl">03 December 2024 13:49:25</div>

FIG. 4. (a) Reverse J–V characteristics of example Ni (green), Pd (blue), and Pt (purple) SBDs with numerical reverse leakage model fits overlaid (solid). (b) Forward J–V characteristics of example Ni, Pd, and Pt SBDs with TFE model fits overlaid.

agreement of reverse J–V characteristics and the numerical tunneling model is shown in Fig. 4(a). The extracted values of $\phi_{B,RIV}$ for Ni, Pd, and Pt are 1.10 ± 0.11, 1.44 ± 0.01, and 1.33 ± 0.02 eV, respectively.

V. DISCUSSION

A. Fermi-level pinning?

Figure 5 plots the extracted barrier heights for Al, Ti, Cr, Ni, Pd, and Pt on Ga_2O_3 vs their respective metal work function with prior published data. Prior studies imply that the measured barrier height on Ga_2O_3 is heavily pinned and collectively demonstrate a minimal dependence on the work function of the contact metal. In this work, overall, we observe $\phi_{Al} < \phi_{Ti} < \phi_{Cr} < \phi_{Ni} < \phi Pt < \phi_{Pd}$, which trends with increasing ϕ_M with the exception of Pd and Pt (5.4 vs 5.65 eV), which are reversed. Fitting these
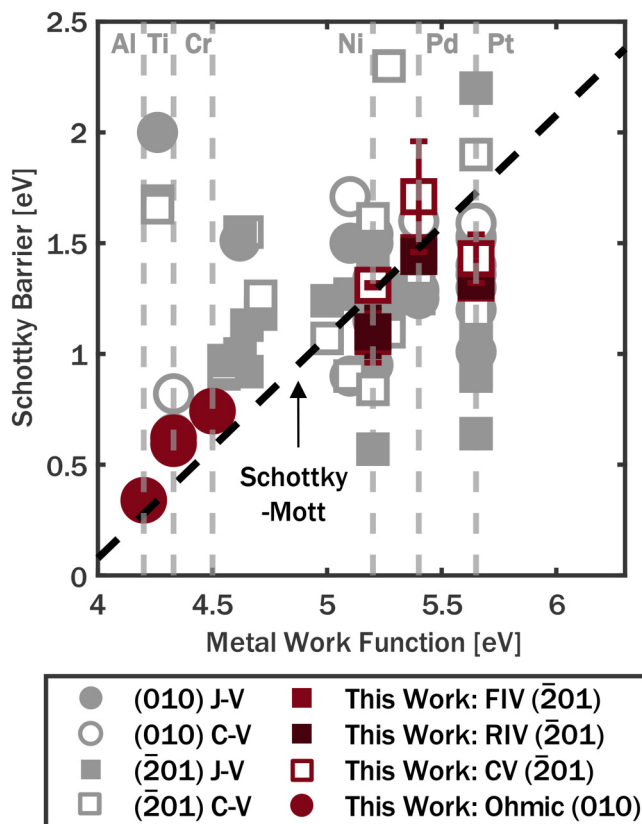

FIG. 5. Measured ϕ_B vs ϕ_M from the literature (gray) and this work (red). Only the orientations used in this work, (010) and ($\bar{2}$01) are included, with the data sorted by surface orientation and the type of measurement. This work shows ϕ_B largely increases with increasing ϕ_M, while measurements from the literature show significant Fermi-level pinning. Values from the literature and associated references are tabulated in the supplementary material. The overall S value based on this work alone (the red symbols) is 0.66 ± 0.03, and R^2 of 0.77 though the fitted line is not shown in this plot.

extracted barriers to the modified Schottky–Mott rule in Eq. (2) gives $S = 0.7 ± 0.2$ with an R^2 of 0.85. For the barriers extracted by multiple methods, as is often observed, the barrier heights extracted by C–V are slightly higher than the barriers extracted from forward and reverse J–V.[25] The barrier heights, however, obey the same trend for all barrier height extraction methods.

Surface orientation and interface chemistry may both play a role in the observation of S-values less than 1. Previous work has indicated that Fermi-level pinning and Schottky barrier height can depend on the surface crystal orientation due to the low level of crystal symmetry in Ga_2O_3, which results in different surface energies and density of surface states.[26] On the (100) surface of Ga_2O_3, for example, Lyle et al. demonstrated a significantly lower amount of Fermi-level pinning with S values ranging from 0.7 to 0.97, while Lingaparthi et al. obtained a similar value of $S \sim 0.66$ on the (001) surface.[27,28] In contrast, Hou et al. observe near complete Fermi-level pinning ($S \sim 0$) on the ($\bar{2}$01) and (010) surface, which was attributed to the large number of oxygen dangling bonds on this face.[6] On the (010) surface, Farzana et al. do observe a spread of Schottky-barrier heights, though they do not trend as predicted by the Schottky–Mott rule (albeit within a fairly small data set), indicating that Fermi-level pinning may not dominate Schottky-barrier formation.[29] Our observation of a positive S value of ~0.7 indicates that apparent Fermi-level pinning can at least be somewhat alleviated by processing techniques that preserve as-grown interface quality even on these historically pinned surface orientations. However, as this work does span two different crystal orientations, (010) and ($\bar{2}$01), further work should investigate more closely Fermi-level pinning on different orientations with identical process conditions.

B. Contact oxidation: XPS

As stated previously, Fig. 5 is plotted using the *metal* work function, not necessarily the work function of the metal or metal oxide present at the metal–semiconductor interface that ultimately yields the electrical contact. As shown in the prior literature, oxidation does increase the work function of stoichiometric and non-stoichiometric metal oxides and may, at least partially, account for the non-unity values of S.[30,31] Extracting the *exact* work function of these non-stoichiometric metal oxides is outside the scope of this study, except to note that their presence indicates an increase in the work function that may adjust ϕ_B of metals, such as Ti and Cr (Fig. 4), to be aligned with the Schottky–Mott model. To further investigate oxidation as a source of non-ideal S values, we performed depth-resolved XPS measurements of the oxidation state of each contact metal at the contact-Ga_2O_3 interface. The depth profiles are shown in Fig. 6. Despite all contacts not receiving a post-deposition anneal or thermal processing exceeding 200 °C for photoresist processing, the majority of the contact metals are at least partially oxidized. Due to the deposition occurring under ultrahigh vacuum pressures of 10^{-7} Torr, it is unlikely that the deposited metal was oxidized by oxygen during the line-of-site e-beam evaporation; oxidation is more likely due to a redox reaction with the underlying Ga_2O_3.[32] As expected, those metal oxides with the lowest free energy of formation at room temperature [i.e., Al_2O_3, TiO_2, and Cr_2O_3, Figs. 6(a)–6(c)] show significantly more
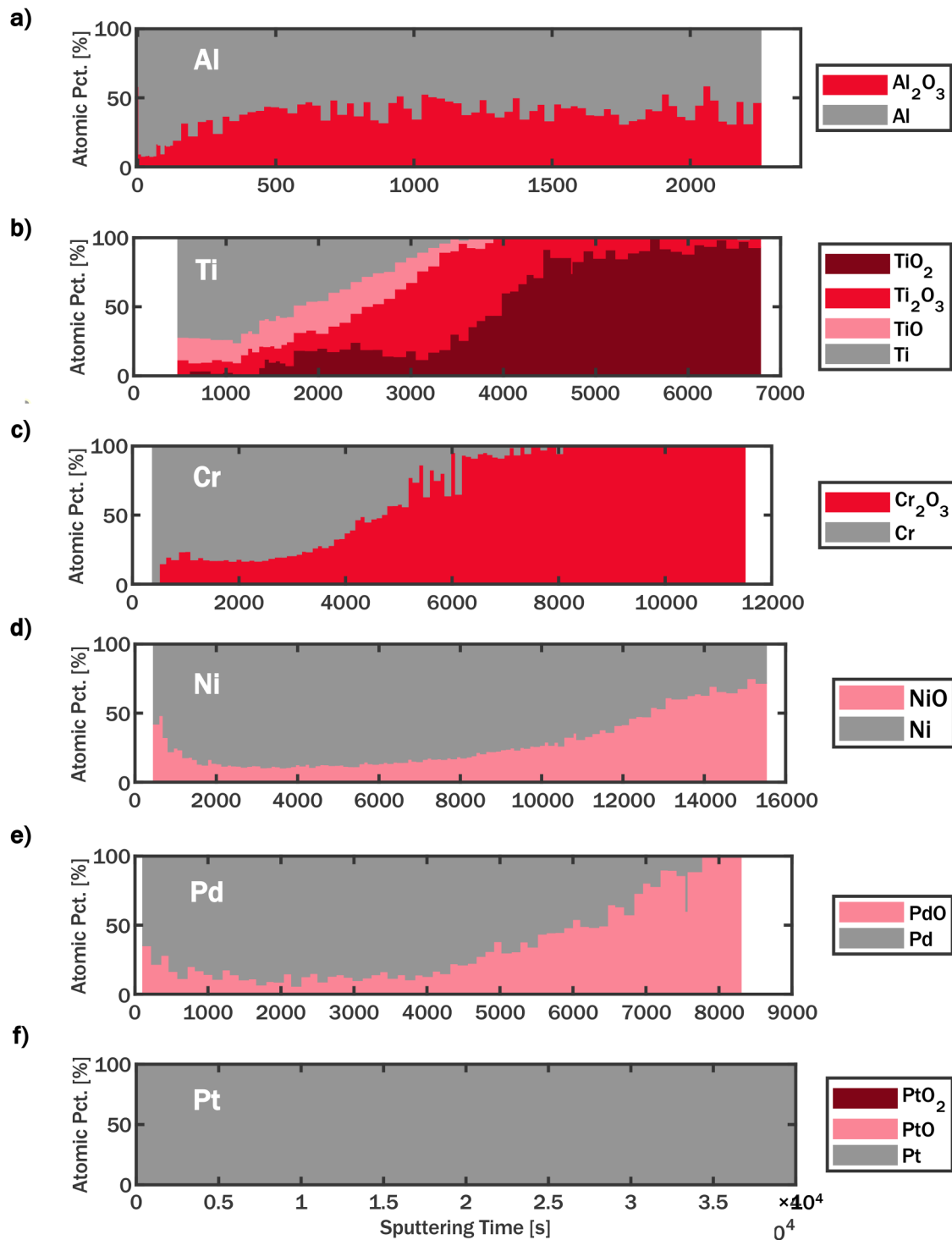
FIG. 6. Depth profiles of oxidation states of contact metals for (a) Al, (b) Ti, (c) Cr, (d) Ni, (e) Pd, and (f) Pt on β-Ga$_2$O$_3$ from decreasing to increasing energy of oxide formation. At room temperature, Ti and Cr are almost completely oxidized to TiO$_2$ and Cr$_2$O$_3$, respectively, while Al, Ni, and Pd are partially oxidized to Al$_2$O$_3$, NiO, and PdO, and Pt is entirely unoxidized.

oxidation than the metal oxides with higher energy of formation [i.e., NiO, PdO, PtO$_2$, Figs. 6(d)–6(f)].[33]

As the metals with the lowest ϕ_M are also the metals that are most prone to oxidation and, therefore, most likely to experience an increase in the work function, the apparent Fermi-level pinning and low S values observed in metal Schottky contacts to Ga$_2$O$_3$ may be attributed to under-reporting the work function of these oxidized and partially oxidized layers, in addition to any adverse effect that conventional processing may have introduced to the interface—most of the reports in the literature to date with the exception of Carey *et al.* and Cromer *et al.* have used a liftoff process. This could also explain the discrepancy between ϕ_M and ϕ_B observed for Pd and Pt, as the Pd layer is partially oxidized and may, therefore, have a higher work function than reported. Precise measurement and understanding of the value of the work function for partially oxidized and oxidized metal contacts is beyond the scope of this work. Future studies of barrier height extraction ought to be mindful of the significant influence of minute changes in E_c relative to ϕ_M from bandgap renormalization for accurate barrier height determination.

VI. CONCLUSIONS

In conclusion, we report non-alloyed metal-first ohmic and Schottky contacts on β-Ga$_2$O$_3$ with a range of contact metal work functions. We attain an ultralow contact resistance of $0.069 \pm 0.003\,\Omega$ mm with Al contacts. Furthermore, we extract values for the Schottky-barrier height from the I–V characteristics of TLM patterns for the lower work-function metals and SBDs for the higher work-function metals. The extracted values of ϕ_B largely increase with increasing ϕ_M with an S value of 0.7 ± 0.2, indicating that the Fermi-level may at least somewhat be un-pinned by metal-first processing that preserves the bare-substrate ($\bar{2}01$) and as-grown (010) surfaces in contrast with historical reports showing complete Fermi-level pinning on the ($\bar{2}01$) and (010) surfaces. Depth-resolved XPS investigation of the oxidation state of the contact metals indicates that the majority of contact metals are at least partially oxidized even without alloying, which may result in higher work functions than reported and partially explain the persistence of apparent Fermi-level pinning. Further understanding of the crystal orientation dependence coupled with the precise effect of the oxidation state on work function may assist in further un-pinning the Fermi-level in β-Ga$_2$O$_3$ and improving quality and consistency of Schottky and ohmic metal contacts.

SUPPLEMENTARY MATERIAL

See the supplementary material for additional sample growth details and processing details, an expanded discussion of Burstein–Moss and bandgap renormalization, illustrations of the criteria distinguishing between the TE and TFE regimes, details of the numerical tunneling model used to fit the reverse IV of the SBDs, and tabulated historical Schottky-barrier height measurements.

ACKNOWLEDGMENTS

AUTHOR DECLARATIONS

Conflict of Interest

The authors have no conflicts to disclose.

Author Contributions

Kathleen T. Smith: Conceptualization (lead); Data curation (lead); Formal analysis (lead); Investigation (lead); Methodology (lead); Validation (equal); Visualization (lead); Writing – original draft (lead); Writing – review & editing (equal). **Cameron A. Gorsak:** Investigation (supporting); Resources (equal); Writing – review & editing (equal). **Joshua T. Buontempo:** Investigation (supporting); Resources (equal). **Bennett J. Cromer:** Formal analysis (supporting); Visualization (supporting); Writing – review & editing (equal). **Takumi Ikenoue:** Funding acquisition (supporting); Supervision (supporting). **Hemant Gulupalli:** Investigation (supporting). **Michael O. Thompson:** Funding acquisition (equal); Supervision (equal). **Debdeep Jena:** Funding acquisition (equal); Supervision (equal). **Hari P. Nair:** Funding acquisition (equal); Supervision (equal). **Huili Grace Xing:** Conceptualization (equal); Data curation (equal); Formal analysis (equal); Funding acquisition (lead); Methodology (equal); Supervision (equal); Validation (equal); Writing – review & editing (equal).

DATA AVAILABILITY

The data that support the findings of this study are available from the corresponding authors upon reasonable request.

REFERENCES

[1]M. Higashiwaki, K. Sasaki, A. Kuramata, T. Masui, and S. Yamakoshi, Appl. Phys. Lett. **100**, 013504 (2012).

[2]A. J. Green, J. Speck, G. Xing, P. Moens, F. Allerstam, K. Gumaelius, T. Neyer, A. Arias-Purdue, V. Mehrota, A. Kuramata, K. Sasaki, S. Watanabe, K. Koshi, J. Blevins, O. Bierwagen, S. Krishnamoorthy, K. Leedy, A. R. Arehart, A. T. Neal, S. Mou, S. A. Ringel, A. Kumar, A. Sharma, K. Ghosh, U. Singisetti, W. Li, K. Chabak, K. Liddy, A. Islam, S. Rajan, S. Graham, S. Choi, Z. Cheng, and M. Higashiwaki, APL Mater. **10**, 029201 (2022).

[3]K. N. Heinselman, D. Haven, A. Zakutayev, and S. B. Reese, Cryst. Growth Des. **22**, 4854–4863 (2022).

[4]Z. Xia, H. Chandrasekar, W. Moore, C. Wang, A. J. Lee, J. McGlone, N. K. Kalarickal, A. Arehart, S. Ringel, F. Yang, and S. Rajan, Appl. Phys. Lett. **115**, 252104 (2019).

[5]N. K. Kalarickal, Z. Xia, H.-L. Huang, W. Moore, Y. Liu, M. Brenner, J. Hwang, and S. Rajan, IEEE Electron Device Lett. **42**, 899–902 (2021).

[6]C. Hou, R. M. Gazoni, R. J. Reeves, and M. W. Allen, Appl. Phys. Lett. **114**, 033502 (2019).

[7]B. Cromer, D. Saraswat, N. Pieczulewski, W. Li, K. Nomoto, F. V. E. Hensling, K. Azizie, H. P. Nair, D. G. Schlom, D. A. Muller, D. Jena, and H. G. Xing, J. Vac. Sci. Technol. A **42**, 033206 (2024).

[8]L. A. M. Lyle, J. Vac. Sci. Technol. A **40**, 060802 (2022).

[9]J. A. Spencer, A. G. Jacobs, A. D. Hobart, K. D. Koehler, T. J. Anderson, Y. Zhang, and M. J. Tadjer, J. Electron. Mater. **53**, 2798–2805 (2024).

[10]M. E. Islam, K. Shimamoto, T. Yoshimura, and N. Fujimura, AIP Adv. **14**, 045003 (2024).

[11]S. Kurtin, T. C. McGill, and C. A. Mead, Phys. Rev. Lett. **22**, 1433–1436 (1969).

[12]R. T. Tung, Appl. Phys. Rev. **1**, 011304 (2014).

[13]K. T. Smith, C. A. Gorsak, A. Kalra, B. J. Cromer, K. Azizie, D. M. Dryden, D. G. Schlom, D. Jena, H. P. Nair, and H. G. Xing, Appl. Phys. Lett. **123**, 242101 (2023).

[14]I. Carey, H. Patrick, J. Yang, F. Ren, D. C. Hays, S. J. Pearton, S. Jang, A. Kuramata, and I. I. Kravchenko, AIP Adv. **7**, 095313 (2017).

[15]I. Carey, H. Patrick, J. Yang, F. Ren, D. C. Hays, S. J. Pearton, A. Kuramata, and I. I. Kravchenko, J. Vac. Sci. Technol. B **35**, 061201 (2017).

[16]J. P. McCandless, C. A. Gorsak, V. Protasenko, D. G. Schlom, M. O. Thompson, H. G. Xing, D. Jena, and H. P. Nair, Appl. Phys. Lett. **124**, 111601 (2024).

[17]J. Zhang, J. Willis, Z. Yang, Z. Sheng, L.-S. Wang, T.-L. Lee, L. Chen, D. O. Scanlon, and K. H. L. Zhang, Phys. Rev. B **106**, 205305 (2022).

[18]C. Chang, Y. Fang, and S. Sze, Solid State Electron. **14**, 541–550 (1971).

[19]W. Li, D. Saraswat, Y. Long, K. Nomoto, D. Jena, and H. G. Xing, Appl. Phys. Lett. **116**, 192101 (2020).

[20]S. Bharadwaj, S. M. Islam, K. Nomoto, V. Protasenko, A. Chaney, H. G. Xing, and D. Jena, Appl. Phys. Lett. **114**, 113501 (2019).

[21]F. A. Padovani and R. Stratton, Solid State Electron. **9**, 695–707 (1966).

[22]C. Crowell and V. Rideout, Solid State Electron. **12**, 89–105 (1969).

[23]W. Li, D. Jena, and H. G. Xing, J. Appl. Phys. **131**, 015702 (2022).

[24]E. L. Murphy and R. H. Good, Phys. Rev. **102**, 1464–1473 (1956).

[25]J. H. Werner and H. H. Güttler, J. Appl. Phys. **69**, 1522–1533 (1991).

[26]S. Mu, M. Wang, H. Peelaers, and C. G. Van de Walle, APL Mater. **8**, 091105 (2020).

[27]L. A. M. Lyle, K. Jiang, E. V. Favela, K. Das, A. Popp, Z. Galazka, G. Wagner, and L. M. Porter, J. Vac. Sci. Technol. A **39**, 033202 (2021).

[28]R. Lingaparthi, Q. T. Thieu, K. Koshi, D. Wakimoto, K. Sasaki, and A. Kuramata, Appl. Phys. Lett. **116**, 092101 (2020).

[29]E. Farzana, Z. Zhang, P. K. Paul, A. R. Arehart, and S. A. Ringel, Appl. Phys. Lett. **110**, 202102 (2017).

[30]M. T. Greiner and Z.-H. Lu, NPG Asia Mater. **5**, e55 (2013).

[31]K. P. Kepp, ChemPhysChem **21**, 360–369 (2020).

[32]M.-H. Lee and R. L. Peterson, ECS J. Solid State Sci. Technol. **8**, Q3176–Q3179 (2019).

[33]H. J. T. Ellingham, Trans. Commun. J. Chem. Technol. Biotechnol. **63**, 125–160 (1944).